Title
Brightness of Microtrench Superhydrophobic Surfaces and Visual Detection of Intermediate Wetting States.

Permalink
https://escholarship.org/uc/item/088309bk

Journal
Langmuir : the ACS journal of surfaces and colloids, 37(3)

ISSN
0743-7463

Authors
Yu, Ning
Kiani, Sarina
Xu, Muchen
et al.

Publication Date
2021-01-11

DOI
10.1021/acs.langmuir.0c03172

Supplemental Material
https://escholarship.org/uc/item/088309bk#supplemental

Peer reviewed

Brightness of Microtrench Superhydrophobic Surfaces and Visual Detection of Intermediate Wetting States

Ning Yu[1,], Sarina Kiani[1], Muchen Xu[1], and Chang-Jin "CJ" Kim[1,2,3]*

[1]Mechanical and Aerospace Engineering Department

[2]Bioengineering Department

[3]California NanoSystems Institute (CNSI)

University of California, Los Angeles (UCLA), Los Angeles, CA 90095, USA.

ABSTRACT

For a superhydrophobic (SHPo) surface under water, the dewetted or wetted states are easily distinguishable by the bright silvery plastron or lack of it, respectively. However, to detect an intermediate state between the two, where water partially intrudes the surface roughness, a special visualization technique has been needed. Focusing on SHPo surfaces of parallel microtrenches and considering drag reduction as a prominent application, we (i) show the reliance on surface brightness alone may seriously mislead the wetting state, (ii) theorize how the brightness is determined by water intrusion depth and viewing direction, (iii) support the theory experimentally with confocal microscopy and CCD cameras, (iv) present how to estimate the intrusion depth using optical images taken from different angles, and (v) showcase how to detect intermediate states slightly off the properly dewetted state by simply looking. The proposed method would allow monitoring SHPo trench surfaces without bulky instruments – especially useful for large samples and field tests.

INTRODUCTION

A superhydrophobic (SHPo) surface would transition from the dewetted to wetted state when water intrudes into the surface roughness or from the wetted to dewetted state when the trapped air grows in the roughness, depending on hydrostatic pressure and dissolved air concentration, among others[1]. The transitions may be categorized by the position of the air-water-solid contact lines, as schematically illustrated in Figure 1, where the roughness is drawn as a regular microstructure for simplicity and the states of overgrown air above the roughness are added to be complete. Because most underwater applications of SHPo surfaces, such as drag reduction[2,3,4,5] and antibiofouling[6,7], require the surface roughness to be substantially filled with an air layer, called plastron[8], it is highly desirable that the SHPo surface stays dewetted under water. Since the

overgrowing air, Figure 1(b), usually causes the contact-lines to detach from the surface, leading to the overly dewetted state of Figure 1(a), which is unstable, for most applications the desired state is the properly dewetted state of Figure 1(c), which is commonly regarded as Cassie-Baxter state. We said "commonly" because Figures 1(b) and 1(d) also belong to the composite interface considered by Cassie and Baxter[9,10]. This rather casual and imprecise naming of the pinned state as Cassie-Baxter state is widespread because the intermediate states are usually not apparent or addressable and simply ignored.
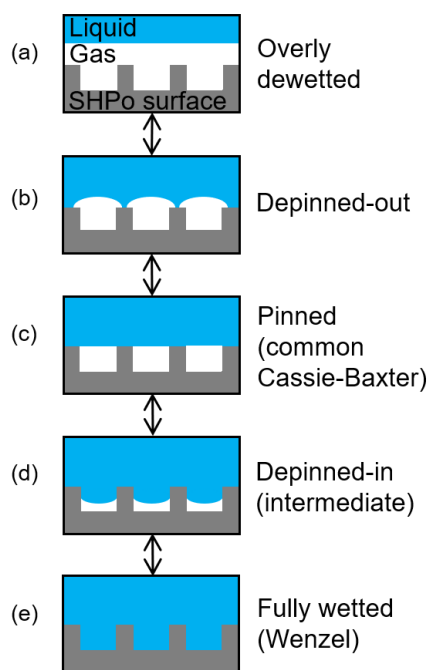
Figure 1. Various wetting states of a submerged SHPo surface categorized by the degree of wetting, adapted from Lee, Choi, and Kim[2]. The current report aims to detect the depinned-in state (d), which is intermediate between the pinned state (c) and the fully wetted state (e), on microtrench SHPo surfaces. The depinned-in state (d) can appear either silvery bright like the pinned (c), dark black like the fully wetted (e), or greyish between bright and dark, depending on the water intrusion depth and observer's viewing directions. The overly dewetted state (a) and depinned-out state (b) are not considered in this report.

Most times, the dewetted states, Figure 1(a-d), are visually distinguishable by the bright silvery sheen due to the total internal reflection (TIR) of light at the water-air interface. In contrast, the fully wetted states, Figure 1(e), known as Wenzel[11] state appears dark, because with no water-air interface light reaches the inner surfaces of the surface roughness and gets scattered. This first-order information whether the SHPo surface is dewetted (appearing bright) or fully wetted

(appearing dark) are good enough for some applications, where the intermediate states between the dewetted and fully wetted states are transient and ignorable. However, for other applications, where the intermediate states are important and not transient, the second-order information, such as the intermediate state of wetting shown in Figure 1(d), may further be necessary. For example, the intermediate wetting state with the air-water contact line depinned from the roughness top edge, as illustrated by Figure 1(d), may persist instead of jumping to the fully wetted state of Figure 1(e) in some hydrodynamic conditions[2,12]. In particular, recent studies found that, while both may appear bright, the pinned state of Figure 1(c) may entail significant drag reduction but the depinned-in state of Figure 1(d) may not and even invoke drag increase[13,14] expected of the fully wetted state of Figure 1(e), leading to some inexplicable results in the field of SHPo drag reduction[2]. To avoid such a major pitfall, one needs to know which sub-states of the dewetted state (while all appearing bright) a SHPo surface is in. More specifically, this paper seeks to distinguish the depinned-in state of Figure 1(d) from the pinned state Figure 1(c) on a SHPo surface made of parallel microtrenches. Furthermore, we show the depth of water intrusion can be quantitatively estimated by observing the sample surface with a series of viewing angles. The other intermediate wetting state, i.e., the depinned-out state (Figure 1(b)) which is between the pinned state (Figure 1(c)) and the overly dewetted state (Figure 1(a)), is not considered in this report.

Over the past decade, numerous methods have been utilized or developed to find the shape and position of the water-air interface on SHPo surfaces. The most widely used for its convenience is by the bright silvery appearance, which simply indicates the existence of plastron on an immersed SHPo surface[15,16,17,18,19], i.e., Figure 1(a-d). Additional details would require some instrumentation. Rathgen et al.[20] measured the diffraction pattern of reflected light to detect the detailed meniscus shape on parallel microtrenches. Acoustic sensing[21,22,23], quartz crystal microbalance[24], micro particle image velocimetry[25], and transmission small-angel x-ray scattering[26] were utilized to detect the intrusion depth (wetting depth) of water into surface roughness. On the other hand, a variety of strategies have been used for more direct visualization of the water-air interface on SHPo surface, including optical microscopy[1,27,28], confocal microscopy[29,30,31], interference microscopy[32], atomic force microscopy[33,34,35], environmental scanning electron microscopy (SEM)[36], X-ray computed tomography[37,38], and freeze fracturing approach[39,40]. Unfortunately, however, they are not suitable or convenient for large samples or general field studies (e.g., boat on the sea[4], model in a tow tank[41,42], where the SHPo surface of interest may travel at high speed under water and cannot accommodate installation of any bulky instrument.

Considering field experiments of SHPo drag reduction[4] as a prominent example, in this paper we propose and confirm a strategy to detect the intermediate wetting – distinguish the depinned-in state (Figure 1(d)) from the pinned state (Figure 1(c)) in particular – on SHPo surfaces without special instrumentation. Periodic microtrenches aligned to the flow direction are of the prime interest because they have recorded the largest slip lengths (up to 400 µm)[43], the largest drag reductions in water tunnel (up to 75%)[44], and so far the only successful drag reduction (~30%) under turbulent flows in open water[4,42]. This work was initiated by our long frustration while trying to interpret the results in the literature without knowing whether the bright plastron reported in most of the successful experiments was indeed in the depinned state Figure 1(c) or mixed with the depinned-in state of Figure 1(d)[2]. More specifically, for an amount of drag reduction reported, how much of the SHPo surface was bright and properly dewetted (i.e., pinned) to fully contribute to drag reduction and how much was also bright but in intermediate states to compromise the reduction? The strategy proposed in this paper to address this challenge was based on our own disturbing experience that a depinned-in state with a relatively small but non-negligible intrusion depth would appear as bright as the pinned state and motivated by our impromptu observation that the same surface could appear dark if seen with a very small elevation angle. Encouraged by a qualitative proof-of-concept with naked eyes[45], in this report we first establish a geometric model that mathematically relates how the surface brightness is affected by the water intrusion depth and observer's viewing angles and then perform a series of viewing tests using three underwater cameras and a confocal microscope simultaneously to quantitatively assess the proposed scheme. The strategy is being utilized for our flow studies in field conditions, following the recent report of SHPo drag reduction tested under a 13 foot motorboat in open sea[4] – an exemplary field condition.

THEORETICAL SECTION

The Model. Between the pinned (i.e., common Cassie-Baxter) state of Figure 1(c) and the fully wetted (i.e., Wenzel) state of Figure 1(e) under water, a SHPo surface would appear the brightest at the former and the darkest at the latter. Since SHPo surfaces appear bright by the total internal reflection (TIR) off the water-air interface on the plastron, let us simplify the discussion by assuming TIR dominates the light reaching the viewer, i.e., ignoring all other lights, for now. To explain the underlying concept and proposed strategy, it helps to define the observation direction of a viewer (e.g., camera, person) with the elevation angle β and azimuth angle φ with respect to the sample surface and transverse trench direction, respectively. Figure 2(a) shows β and φ in a rectangular coordinate system, where x direction is parallel to the trenches, y direction

4

is normal to the sample surface, and z direction is transverse to the trenches, with the coordinate origin as the center of observation and the yellow arrow pointing to the viewer. As far as this report is concerned, the elevation angle is $0 \leq \beta \leq 41.4°$ for TIR on flat water-air interface, and the azimuth angle is $0 \leq \varphi \leq 90°$ due to the symmetry of parallel trenches. In addition to assuming (i) TIR dominates the light, we further assume: (ii) the water-air interface is flat inside the trench, (iii) the lighting is diffusive, and (iv) the viewer is far from the surface so that the observation angles are uniform throughout the surface of interest. The first and second assumptions will be discussed later in this section, and the third and fourth assumptions will be explained in the next section. For a SHPo surface with periodic trenches, let us define their pitch (periodicity) is p, width is w, and depth is d. Figure 2(b) shows a trench cross-sectioned along the plane of incidence, defining azimuthal pitch $p' = p/\cos\varphi$ and azimuthal width $w' = w/\cos\varphi$. Note that the azimuthal width of trench coincides with the actual width when $\varphi = 0°$ and increases with φ. The degree of water intrusion into the trench, i.e., intrusion depth h, is defined as the vertical distance between the trench top edge and the solid-water-air three-phase contact line on the trench sidewall. The intrusion depth h can be normalized by the trench depth d as intrusion ratio $h^* = h/d$ so that the pinned state has $h^* = 0$, the depinned-in state has $0 < h^* < 1$ and the fully wetted state has $h^* = 1$. Since the sidewalls (assuming an opaque material) of trench would block the light, as shown in Figure 2(b), the portion of meniscus available for TIR to the viewer for a given observing direction is w_T'. The meniscus width providing TIR can be expressed as:

$$w_T' = w' - \frac{h}{tan\beta} \tag{1}$$

Brightness Ratio. The brightness μ (seen to the viewer) of a microtrench SHPo surface under water would be determined by the areal ratio between the meniscus of TIR visible to the viewer and the entire SHPo surface, i.e., w_T'/p', because for now all other areas of the surface are assumed to appear completely dark. Furthermore, for this report it is more relevant and useful to express the brightness relative to the brightness possible on a given SHPo surface, i.e., with a given gas fraction (w/p), i.e., as the bright ratio:

$$\mu^* = \frac{\mu - \mu_{fully\ wetted}}{\mu_{pinned} - \mu_{fully\ wetted}} = \frac{w_T}{w} = w_T^* \tag{2}$$

where μ_{pinned} and $\mu_{fully\ wetted}$ indicate the brightness of the pinned and the fully wetted state, respectively. For a given SHPo surface and excluding the depinned-out or overly dewetted from consideration, the pinned state (Figure 1(c)) would appear the brightest, i.e., $\mu^* = 1$, because all of the water-air menisci on the SHPo surface sends TIR light to the viewer, while the fully wetted

5
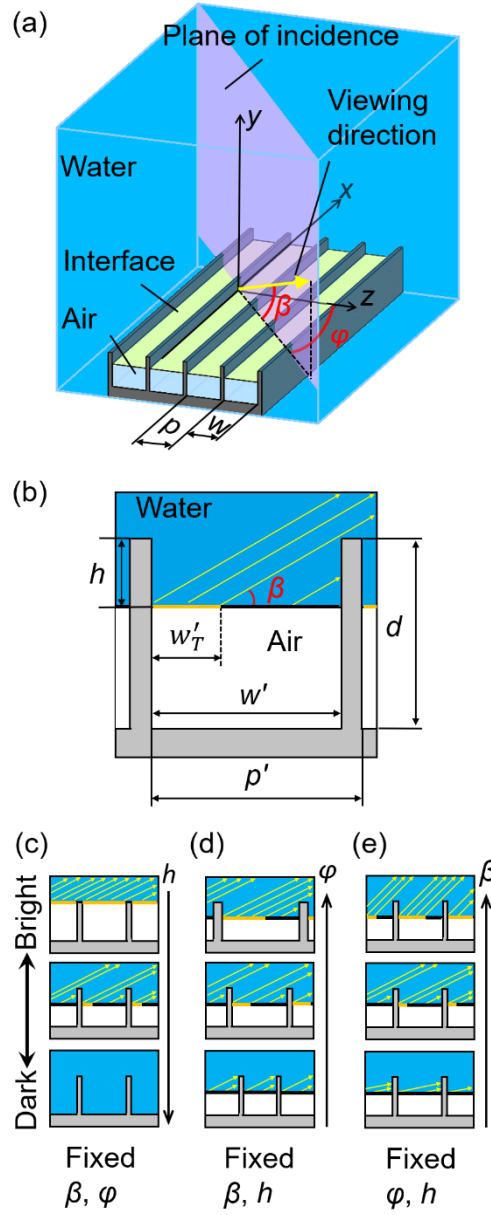
Figure 2. The proposed relationship between the viewing direction and surface brightness of a microtrench SHPo surface. (a) The viewing direction (yellow arrow) is defined by two angles: elevation angle β with respect to the sample surface (xz plane) and azimuth angle φ of the incidence plane to the transverse trench direction (z axis). The trenches have pitch p and width w. Drawn not to scale for clarity. (b) The water-air interface inside a trench cross-sectioned along the plane of incidence. The yellow arrows indicate TIR off the meniscus towards the viewer. The red portion would be visible and appear bright to the viewer. (c) TIR towards the viewer for pinned, depinned-in, and fully wetted state. (d, e) TIR towards the viewer detailed for a depinned-in state shows the effect of azimuth angle φ (d) and elevation angle β (e).

state (Figure 1(e)) would appear the darkest, i.e., $\mu^* = 0$, because there is no meniscus for TIR. Accordingly, we define TIR ratio w_T^* as the TIR region w_T relative to the entire meniscus w, i.e., $w_T^* = w_T'/w' = w_T/w$, and the brightness ratio equals the TIR ratio by definition, i.e., $w_T^* = \mu^*$.

During the intermediate state (Figure 1(d)) transitioning from the pinned to fully wetted state, for a given observing direction, the depinned-in state gradually changes from bright to dark since w_T^* decreases when meniscus slides down into trench, as shown in Figure 2(c). If w_T^* is large enough to make the surface appear quite bright, the intermediate surface is perceived to be dewetted, i.e., $\mu^* \sim 1$. If w_T^* becomes small enough to make the surface quite dark, the intermediate surface is perceived to be fully wetted, i.e., $\mu^* \sim 0$. This simple choice of either depinned or fully wetted has been widely adopted in practice without any better options unless special instrumentation was used.

Observation Angles. The brightness of depinned-in state is affected not only by the water intrusion depth but also by the observing directions. Figure 2(d) illustrates, for a given intrusion depth h and elevation angle β, that the surface will appear from dark to bright as the azimuth angle φ increases because the TIR ratio w_T^* increases. Similarly, Figure 2(e) illustrates, for a given intrusion depth h and azimuth angle φ, that the surface will appear from dark to bright as the elevation angle β increases because w_T^* increases. These brightness changes by elevation angle and azimuth angle are animated in Video S1 and Video S2, respectively, in Supplementary Information.

Recall the first assumption for the above theory that all the lights reaching the viewer are from TIR, ignoring all other lights. However, since other lights are often not negligible (for example, the solid surfaces on the trench top and sidewall may not be completely dark), a deviation from the above theory is expected. Regarding the fully wetted state, the 30-40% reflection on the silicon surface in water[46] is much weaker than the 100% reflection by TIR on the water-air interface but still significant. However, in most cases the light reflects off the water-silicon interface multiple times (e.g., reflections on sidewall, bottom, then the other sidewall) before only a few percent reaching the viewer. The main deviation from the negligible non-TIR assumption is for large azimuth angle φ, for which the light may reflect the water-silicon interface only once (on the trench bottom) before 30-40% reaching the viewer, as will be discussed later with the experimental results. Other non-TIR reflections include those on the trench top surfaces, which increase with the solid fraction of SHPo surface, and those on the trench sidewalls above the water-air interface for depinned-in cases, which increases with intrusion depth. For the current study, which employed typical silicon micromachining, the 10% solid fraction of the top surfaces and the roughness on

7

sidewall surfaces make the non-TIR reflection on them negligibly small. While the absolute brightness μ is further affected by various other factors (e.g., reflection on other surfaces around the sample, the exposure of the camera, the background light intensity), what really matters to the observer is the brightness relative to those on the pinned and the fully wetted surface on the same sample location at the same observation event. Accordingly, the brightness ratio μ^* will play a main role in the proposed strategy.

Intrusion Depth vs. Brightness. Utilizing the fact that the pinned state appears the brightest (i.e., $\mu^* = 1$) and the fully wetted state appears the darkest (i.e., $\mu^* = 0$) for any φ and β, let us discuss how the intrusion depth h can be obtained from the brightness ratio μ^* and the observation angles φ and β. Utilizing $w_T^* = \mu^* = w_T'/w'$ and $h^* = h/d$, Equation 1 can be rearranged to be:

$$h^* = (1 - \mu^*)\frac{w \, \tan\beta}{d \, \cos\varphi} \tag{3}$$

where $0 \leq \beta \leq 41.4°$, $0 \leq \varphi < 90°$, $0 \leq \mu^* \leq 1$ and $0 \leq h^* \leq 1$. Equation 3 indicates that, in theory, one can estimate h^* by just measuring μ^* for any viewing direction φ and β. However, in reality, the brightness measurement was found unreliable with scattered data when the brightness ratio was close to the two ends ($\mu^* \sim 0$ or 1), as will be shown later in the experimental results. To avoid the limitation, we propose a better strategy is to assign a target value away from 0 and 1 for μ^* and find φ and β that result in the target value of μ^*. An obvious choice would be a middle point, i.e., $\mu^* = 0.5$, which reduces Equation 3 to:

$$h^* = \frac{w \tan\beta}{2d \, \cos\varphi} \tag{4}$$

In fact, $\mu^* = 0.5$ will be found effective by the experiments in the next sections. In other words, Equation 4 establishes a relationship between intrusion ratio h^* and observing angles β and φ when the surface appears half-bright and half-dark.

When the meniscus bends inwardly by hydrostatic pressure, some region of the meniscus may lose TIR and make the surface darker than the flat meniscus case (i.e., the second assumption), causing the measured brightness to overestimate the intrusion ratio h^*. The overestimation may occur and grow with a larger intrinsic contact angle, larger elevation angle, and small azimuth angle but mostly avoidable in practice, as analyzed in Supplementary Information.

Other SHPo Surfaces. Incidentally, for SHPo surfaces with micro posts or random roughness, which do not have continuous structures to fully block the reflected light, as explained with Figure

S1 in Supplementary Information, the brightness is not affected by the observing direction and cannot be utilized to quantitatively assess the depinned-in state. Lastly, since the underlying concept is based on the substrate material being opaque, the proposed method will need to be modified for SHPo surfaces made of a transparent material[47].

EXPERIMENTAL SECTION

Sample Preparation. A large series of experiments was performed to put the underlying concept and theory formalized above to the test, using SHPo surfaces decorated with periodic microtrenches. After creating depinned-in states at 4 different intrusion ratios, a range of observation directions that make the surface appear to be $\mu^* = 0.5$ were found and compared with the intrusion ratios through Equation 4. The surface sample was made from silicon wafer using deep reactive iron etching (DRIE) with regular photolithography, dicing the wafer to square samples, and spin-coating them with Teflon AF (Chemours), as explained with Figure S2 in Supplementary Information. The 1.3 cm × 1.3 cm sample has a 1.0 cm × 1.0 cm testing area full of microtrenches in the middle, outside which is smooth, as shown in Figure 3(a). The microtrenches have pitch $p = 100$ µm, width $w = 90$ µm, and depth $d \approx 90$ µm. The apparent contact angle of water on the fabricated SHPo surface was measured to be 154° (viewed transverse to the trenches) with tilting angle smaller than 1° to all directions, showing the characteristics of a SHPo surface.

Optical Microscopy. To study the appearance of the microtrench SHPo surface in water, three miniature underwater cameras (7mm 5M Micro USB OTG Endoscope, Ehome) were used, as shown in Figure 3(b). Each camera has an IP 67 rating waterproof cylindrical case with a USB cable to transfer real-time images to computer on-the-go (OTG). The position and tilting of each camera were carefully adjusted so that the sample was within the focal distance and at the center of view for all cameras. The field of view (FOV) of each camera was calibrated with respect to its cylindrical case as explained with Figure S4 in Supplementary Information. Note the *yz* coordinates in Figure 3(b) implies it is drawn for $\varphi = 0°$. In our tests, three cameras were held at three positions of $\beta = 10 \pm 0.3°$, $20 \pm 1°$, $30 \pm 2°$, where the plus-minus deviation covers the width of testing area. By rotating the rotational stage around the y axis, φ can be quickly set to any value between 0° and 90° with ±2° at the two ends of the tested area, following the fourth assumption in the previous section with minimal deviations. For the experiments, the sample was placed on a rotational stage in an acrylic container, which was slowly filled with deionized (DI) water, as shown in Figure 3(b). The fluorescent tubes on ceiling were the main source of lighting during the experiments, and the container was covered with diffuse paper to achieve diffused lighting of the

9

fourth assumption in the previous section. In field condition, such as underneath watercraft below wavy water surface, the sunlight is usually dispersed enough to be considered diffusive. The experimental setup is detailed with Figure S3 in Supplementary Information.
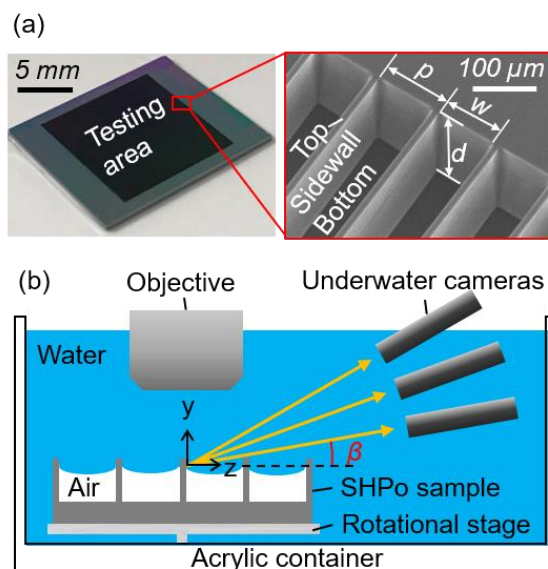
Figure 3. The SHPo sample and experimental setup. (a) Optical image of the prepared SHPo surface sample with parallel microtrenches. The inset SEM image shows an end region of the microtrenches and their pitch *p*, width *w*, and depth *d*. (b) Sketch of the experimental setup consisting of a sample and three cameras (not drawn to scale for clarity). Yellow arrows indicate the directions of cameras observing the sample surface. The objective lens is part of confocal microscope. The cameras are ~8 cm away from the 1 cm × 1 cm testing area. The elevation angle *β* is labeled for the lowest camera.

Controlled Wetting. We achieved several wetting states on one sample and conducted observation tests with large sets of parameters in one immersion, as follows. Water was degassed by boiling it for 30 minutes and cooling it down to room temperature in 2 hours. The air concentration in the prepared water was measured to be ~40% by Total Gas Pressure meter (Point Four™ Tracker, Pentair). The sample was kept at 35 mm below the water surface throughout the immersion tests, letting the gas diffusion between the water and trapped air control the wetting states. The confocal microscopy experiments were performed in a suite specially designed for environmental control (low vibration, air-filtered, air conditioned to ±1°C, light-tight, etc.). Although there was no control system for humidity, the humidity level was measured by a hygrometer and found to be 50% ± 2% throughout the experiments. We generated three different wetting states – pinned, depinned-in, and fully wetted – simultaneously on one sample, as follows.

10

In the water with 40% of air saturation, the trenches immediately started to lose the trapped air, transitioning from the pinned to the depinned-in state. The water-air meniscus slid deeper into the trenches slowly and uniformly with the immersion time, reaching the fully wetted state in about 16 hours for the current trench geometry and air concentration in theory without environmental variation[1]. However, the transition during the test was found to be faster than the theory, i.e. ~3 hours for reaching $h^* = 0.8$, due to the disturbance from handling process when the sample was rotated for imaging. To maintain both a pinned region and a fully wetted region while inducing a depinned-in region with slowly increasing intrusion depth, i.e., all three states simultaneously, on the same sample, we played tricks with a pipette, providing air to locally maintain a pinned state and injecting water to locally create a fully wetted state. After the sample was covered with water at beginning, a ~2 mm-diameter air bubble was pipetted on one region of the sample surface, making the air pockets of several neighboring trenches merge with the pipetted bubble. Replenished of air from the 2 mm bubble as needed by the Laplace pressure, the trenches underneath the bubble remained at a pinned state. If the air bubble was depleted (consumed) before the testing ended, a new air bubble was pipetted on the same location to prolong the pinned state. On the other hand, to create a fully wetted state immediately (vs. otherwise ~16 hours to reach the fully wetted state naturally), water was squirted into microtrenches towards their ends, pushing the trapped air out of the trenches.

Confocal Microscopy. All three wetting states created as described above were analyzed with confocal microscope and observed with three underwater cameras in one experiment. To monitor the meniscus location accurately, i.e., measure the intrusion depth h, a real-time confocal microscope (TCS-SP2-MP-FLIM, Leica) was employed. A U-shape beam was used to allow observation of the meniscus from the top, utilizing a 63× water immersion objective (Leica HCX L APO 63X, WD = 0.9 mm). In one scanning test, the starting plane (the bottom of the meniscus) and the end plane (top of the trenches) were firstly detected and defined manually by adjusting the lens height in z-wide reflection mode (wavelength = 543 nm). Then, a series of spatial images in reflection mode were taken between the two planes and integrated to build the 3D model of meniscus and grating top (i.e., top edge of trenches), from which the exact shape and position of the meniscus could be constructed. Right after each confocal scanning, a series of pictures were taken by three cameras for φ varying from 0° to 90° with 5° intervals, during which the contact line movement was negligible. Since each scanning took 5–10 minutes and the imaging process of camera took ~1 minute, the sliding down of meniscus during the measurement could cause variations of only 0.05 on the measured intrusion ratio h^*. All the pictures taken by the underwater camera were converted to greyscale without any adjustment on contrast and brightness. The

camera exposure settings and background lightings were kept the same during all the tests. One image was taken for each set of 4 water intrusion depths, 3 camera elevation angles, and 19 camera azimuth angles, amounting to 228 sets of test parameters in total. One sample was used to test h^* = 0.24, 0.36, 0.57, and another sample was used to test $h^* = 0.78$. For each of the above 228 images, brightness data from the three wetting states were obtained by reading the average brightness on a region of 3×3 pixels (around 0.5 mm × 0.5 mm) using an image processor (Adobe Photoshop) for each state, amounting to 684 data points in total.

RESULTS AND DISCUSSIONS

Brightness vs. Observation Angles. Among the 12 sets of images collected from the three cameras ($\beta = 10°$, 20°, 30°) to view the four intrusion ratios ($h^* = 0.24$, 0.36, 0.57, 0.78) during the above experiments, the one set for $\beta = 20°$ and $h^* = 0.57$ is presented in Figure 4 as an example. The confocal image of the given intermediate state is shown in Figure 4(a) along with those at the pinned and fully wetted states as references: pinned ($h^* = 0.00$), depinned-in ($h^* = 0.57$), and fully wetted ($h^* = 1.00$). Figure 4(b) presents a series of greyscale pictures taken by the camera at elevation angle $\beta = 20°$ with 10 sequentially varying azimuth angles ($\varphi = 0°$, 5°, 10°, …, 90°). On each of the 10 pictures, where three colored symbols relate the specified portions to the three different wetting states shown in Figure 4(a), brightness was measured for each of the three states. Note the depinned-in state of $h^* = 0.57$ appears as bright as the pinned state at $\varphi = 90°$ but becomes slightly darker at $\varphi = 80°$ and as dark as the fully wetted state when $\varphi < 50°$. The trend shown in Figure 4(b) are corroborated by the animated images from Video S2, as visualized in Figure S5.

To analyze the collected brightness data, the next step is to establish the brightness range (i.e., μ_{pinned} - $\mu_{fully\ wetted}$) for each viewing direction (β, φ) and convert the brightness values μ to brightness ratios μ^* using Equation 2. Figure 5 helps explain this process. Figure 5(a) collects the brightness values μ obtained from Figure 4(b) to reveal the trends of a depinned-in surface ($h^* = 0.57$) as well as the two reference states ($h^* = 0.00$ and $h^* = 1.00$) over the full range of azimuth angle φ at $\beta = 20°$. Note that, whatever φ is, the pinned state ($h^* = 0.00$; green circles) should always appears the brightest (highest μ values), as confirmed in the graph. The fluctuation of its brightness value in the graph is caused mostly by the reflections on sample's rotational stage made of stainless steel – much more than by the none-ITR lights on the sample described in the concept and theorization section. Oppositely, the fully wetted state ($h^* = 1.00$; blue triangle symbols) should always appear the darkest (lowest μ values) as confirmed in the graph. The unreasonable
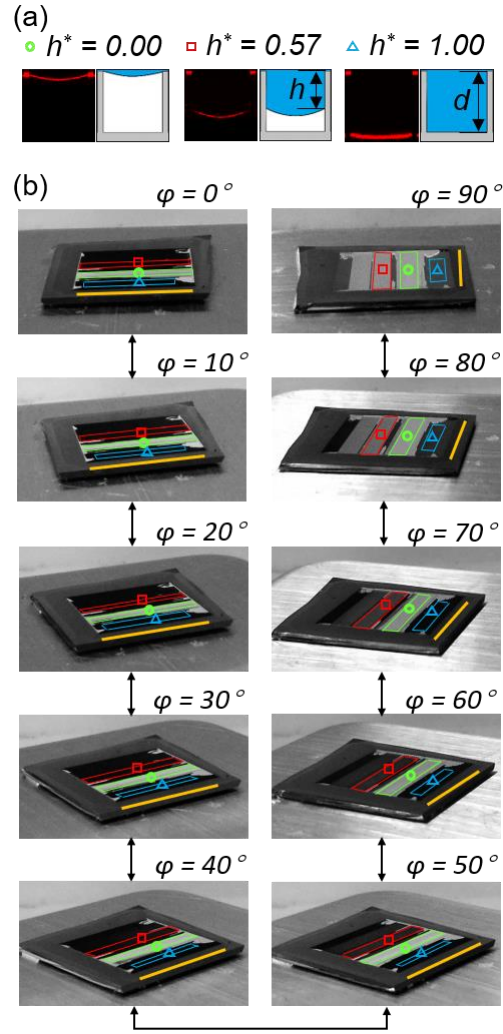
Figure 4. An exemplary set of images over the full range of azimuth angles. (a) Cross-trench profiles of the water-air meniscus in a trench obtained with confocal microscopy are paired with schematic interpretations: pinned state, i.e., $h^* = 0.00$ (left); depinned-in state of $h^* = 0.57$ (middle); and fully wetted state, i.e., $h^* = 1.00$ (right). (b) Greyscale images of the immersed SHPo sample at $h^* = 0.57$ taken by a camera of $\beta = 20°$ are listed over varying azimuth $0° \leq \varphi \leq 90°$. The green circles, red squares, and blue triangles identify the regions of $h^* = 0.00$, 0.57, and 1.00, respectively. The trench directions are indicated by yellow lines. Representing 1 of the 4 intrusion depths tested and recorded by 1 of the 3 cameras used, this set of images is 1 of 12 sets analyzed for this study.

brightness deviation at small azimuth angles ($\varphi > 75°$) is caused by the light reflected from water-silicon interfaces on the trench bottom, as explained as the main deviation from the all-TIR assumption in the theoretical section. In contrast, the depinned-in state ($h^* = 0.57$) appears nearly as bright as the pinned state ($h^* = 0.00$) at $\varphi = 90°$, dims with decreasing φ, and turns nearly as dark as the fully wetted state ($h^* = 1.00$) at sufficiently small φ. More importantly for our purpose, the calculated values of brightness ratio μ^* are presented in Figure 5(b). Since much of the non-TIR reflections, especially those from the surroundings, are shared by all three cases and cancelled out in the brightness ratio μ^*, much of the fluctuation and deviation seen in Figure 5(a) are filtered out in Figure 5(b), explaining the utility of using μ^* instead of μ. Similar trends are found for all of the 12 sets of experiments conducted (i.e., combinatorial sets of $h^* = 0.24, 0.36, 0.57, 0.78$ and $\beta = 10°, 20°, 30°$) as collected in Figures S6 and S7 of Supplementary Information.

The theoretical brightness ratio μ^* is derived from Equation 3 and plotted as solid lines in Figure 5(b) for the same condition as the experiment, i.e., $h^* = 0.57$ at $\beta = 20°$. The sloped line indicates that the brightness of a given intrusion ratio would vary depending on the azimuthal angle φ while it is large enough to provide a viewable TIR, i.e., $w_T^* > 0$. However, without viewable TIR the surface would remain equally dark for all smaller φ as represented by the horizontal line of μ^*. To compare the experiments and theory, in Figure 5(b), the corresponding azimuth angle for surface at $\mu^* = 0.5$ is found to be $71.4°$ theoretically from Equation 4 and $75.5°$ experimentally from data interpolation. The difference of $4.1°$ between them can be attributed to the uncertainties of φ and β in the apparatus and μ^* in data acquisition.

Intrusion Depth vs. Observation Angles. By applying the above process to the 11 remaining sets of results as collected in Figure S7, the intrusion ratio h^* for 12 combinations of β and φ are summarized in Figure 6, where each symbol represents a combination of β, φ and h^*. Figure 6 also includes the theoretical lines from Equation 4 for comparison. Each theoretical line represents one intrusion ratio h^* and indicates the observation directions β and φ that would make the brightness ratio $\mu^* = 0.5$. When the surface with a certain h^* is observed with azimuth angle and elevation angle smaller than the corresponding pair, φ and β, the surface will appear darker, i.e., $\mu^* < 0.5$, and become distinguishable from the dewetted surface. In other words, each φ represents the azimuth angle that starts to make the surface half dark (i.e. $\mu^* = 0.5$) for a given elevation angle β. The similar trends of theory and experiments verify how h^* is related to β and φ. Each line shows the ranges of β and φ that can be used to detect the corresponding h^*. For an example, to detect $h^* = 0.24$, one should use $\beta < 26°$; otherwise, Equation 3 cannot be solved with $\mu^* = 0.5$ and the surface would always appear brighter than $\mu^* = 0.5$. For another example, to detect $h^* = 0.57$, one

14
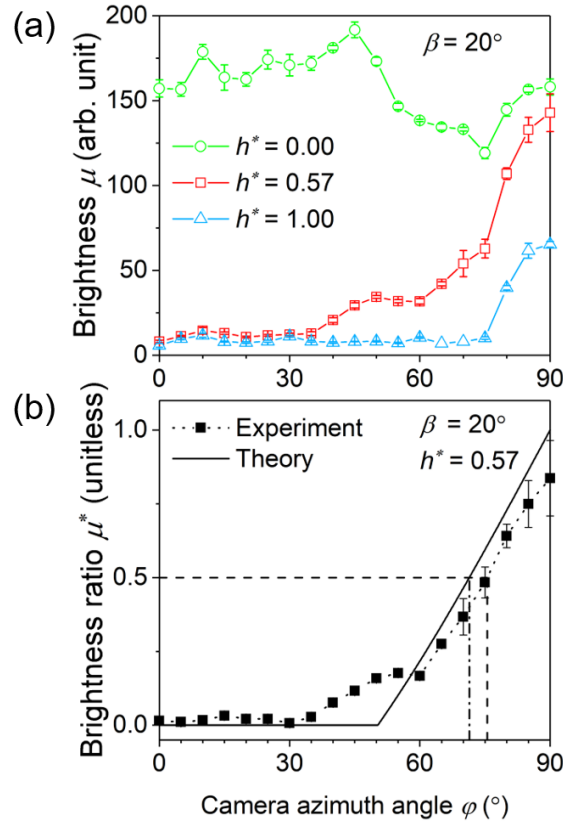
Figure 5. Brightness result obtained for an intermediate (depinned-in) state at intrusion ratio $h^* = 0.57$ with camera elevation angle $\beta = 20°$. (a) Brightness μ on three states $h^* = 0.00, 0.57, 1.00$ measured from the pictures of Figure 4(b). Error bars are statistic error from the standard deviation of brightness data. (b) Brightness ratio μ^* on the depinned-in state of $h^* = 0.57$ relative to the pinned ($h^* = 1.00$) and the fully wetted ($h^* = 0.00$) state. Theoretical predictions (lines) and experimental values (symbols) match despite the reality deviating from the assumptions used for the theory. Dashed and dash-dotted lines relate the experimental and theoretical azimuth angles φ to $\mu^* = 0.5$. Error bars are derived from the standard deviation of brightness data at the corresponding states, as explained in Supplementary Information.

should use $\varphi > 39°$; otherwise, Equation 3 cannot be solved with $\mu^* = 0.5$ and the surface would always appear darker than $\mu^* = 0.5$. Conversely, each observing direction of β and φ has a certain range of intrusion ratio it can detect. For example, with a large β, only relatively large intrusion ratios are detectable (e.g., $0.35 \leqslant h^* < 1$ with $\beta = 30°$), while a smaller β can detect a wider range of intrusion ratios (e.g., $0.11 \leqslant h^* < 1$ with $\beta = 10°$). Accordingly, to detect h^* over as wide range

15

as possible, β should be as small as possible as far as the imaging capabilities (e.g., image resolution) allow. The utilities of the observation map (Figure 6) are discussed in the next section and Supplementary Information.
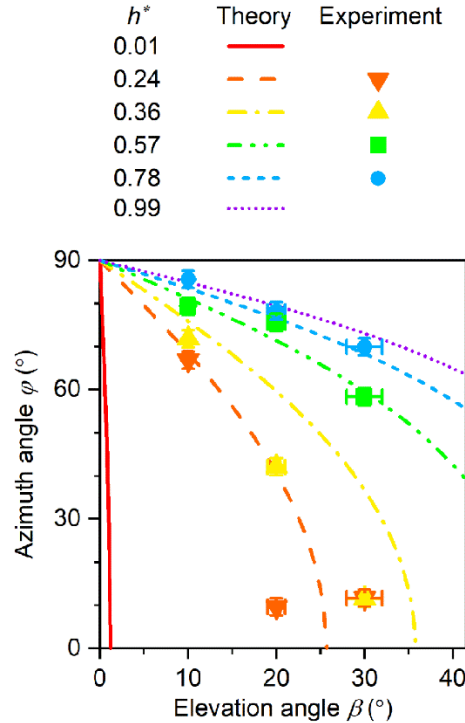
Figure 6. The map of intrusion ratio h^* for observation directions (elevation angle β and azimuth angle φ) using the nominal brightness ratio $\mu^* = 0.5$. Theoretical predictions (lines) for 6 different values of h^* are derived from Equation 4. Experimental data (symbols) of 4 different values of h^* are from all the graphs in Figure S7. The horizontal axis is limited to $0° < \beta < 41.4°$, where TIR exists. The error bars of β and φ are systematic error from the range of angle across the sample area.

Discerning the Pinned vs. Intermediate State. The most prominent application example of this report is to empower one to discern intermediate (i.e., depinned-in) states from the dewetted state on microtrench SHPo surface by simply looking at the surface under water in real time with naked eyes – extremely useful during field experiments. Based on the underlying theory and testing experience, we will first explain the identification principle and then present a step-by-step instruction for the identification. Since differentiation of a depinned-in state from the pinned state becomes more precise as the minimum detectable intrusion depth becomes smaller, the ideal viewing direction is $\varphi = 0°$ and $\beta \sim 0$, which provides the smallest minimum detectable intrusion; in Figure 6, for example, at $\varphi = 0°$ and $\beta = 0.6°$ the minimum detectable intrusion ratio is very small: $h^* = 0.01$. In this condition, any depinned-in state with intrusion ratio larger than the

16

minimum detectable value will appear half dark, which can be easily differentiated from the pinned state (i.e., shiny with $\mu^* = 1$). For $\beta \sim 0$, one should choose the smallest but still functional value in practice. The minimum intrusion depth detectable, according to Equation 4, is $h^* \sim 0.009$ for $\beta = 1°$ and $h^* \sim 0.044$ for $\beta = 5°$, assuming $d = w$. To give a sense of reality, they correspond to $h \sim 0.9$ and 4.4 µm for the trench depth $d = 100$ µm. If larger φ or β is used, the minimum detectable intrusion would be larger. The smallest functional β, which is determined by the trench width and the optical resolution determined by the optical tools, e.g., camera and lighting, was found to be $\sim 5°$ in most practice including the current study. While the nominal value $\mu^* = 0.5$ is used to represent the region of $0 < \mu^* < 1$ when finding h^* from Equation 3 in Figure 6, for naked eyes it is more practical to use $\mu^* = 0$ instead, i.e., determine when the surface appears as dark as fully wetted state rather than half dark.

The above identification procedure can be implemented with the following step-by-step instructions : (1) Before actual tests, create a pinned site and a fully wetted site within the area of interest on the SHPo surface, and get oneself familiar with the appearances of the two reference states with azimuth angle $\varphi = 0°$ and elevation angle $\beta = 5°$ (i.e., a value very close to $0°$ and still practical) under the lighting condition of actual tests. (2) Restore the surface to its natural wetting states and start an actual test. Look at the area of interest with the same observing angles, i.e., $\varphi = 0°$ and $\beta = 5°$. (3) The regions that appear as bright as the pinned site are in a pinned state. The regions that appear as dark as the fully wetted site are not pinned; they are either depinned-in or fully wetted. For uncertainties, variation of azimuth angle caused by unsteady human observation, e.g. $\pm5°$, would not affect the uncertainties of the observation result much. For $\beta = 5°$, the minimum detectable intrusion depth at $\varphi = 5°$ is only 0.3% larger than that at $\varphi = 0°$. However, variation of elevation angle would affect the uncertainties of the observation significantly. For $\varphi = 0°$, the minimum detectable intrusion depth at $\beta \sim 10°$ is twice the depth at $\beta \sim 5°$. By teaching the user to observe the surface with $\varphi = 0°$ and $\beta \sim 0$ with a special care to maintain the elevation angle constant, this method allows one to see which regions are properly dewetted (pinned) and which regions are not (i.e., depinned-in by more than the minimum intrusion depth observable), preventing the common misinterpretation of slightly depinned states as pinned state.

Other Application Examples. Different procedures can be developed for different goals, using the principle and strategy presented in this paper. As a relatively simple example, one can discern intermediate (i.e., depinned-in) states from the fully wetted state by developing a procedure that is opposite but analogous to the above. Using $\varphi = 90°$ and any $\beta < 41.4°$, where the meniscus inside the trench is fully visible to the viewer, a surface that appears similarly dark as the fully

wetted is in the fully wetted state, and a surface that appears distinctively brighter is in either the pinned or a depinned-in state. Combining this method of discerning depinned-in states from the fully wetted state and the preceding method of discerning depinned-in states from the pinned state, one can now determine whether a surface is dewetted, fully wetted, or in an intermediate state between them.

As shown in the preceding section, it is possible to estimate the degree of wetting (i.e., intrusion depth) quantitatively through a more elaborated process, i.e., not by just looking. One such procedure is presented in Supplementary Information along with another procedure that is opposite but analogous. Unlike the simple discerning of depinned-in states from the pinned or fully wetted state, quantitative estimation of the intrusion depth requires the user to take a series of pictures and measure their brightness electronically as performed in the preceding section.

CONCLUSIONS

We have proposed and confirmed a theoretical model to predict the brightness of microtrench SHPo surface under different wetting states by visual observation. The model explained the brightness change on the SHPo surface with the TIR region visible to viewers and how the visible region is affected by the intrusion depth of water and the observation direction defined as elevation angle β and azimuth angle φ. Usual microtrench SHPo surface samples have been fabricated for experiments. After confirming the properly dewetted (i.e., pinned) state appears bright and the fully wetted state appears dark for any observing direction, we verified the model with experiments utilizing confocal microscopy to read the intrusion depths and three underwater cameras to represent visual observations. By quantifying the brightness of surface as function of intrusion depth and observation angles, we provided a strategy to detect the intermediate wetting (depinned-in) state as well, not just the usual but crude information of wetting or dewetting.

ASSOCIATED CONTENT

Supplementary information (PDF)

Elevation angle effect to the brightness animated for 4 intrusion depths (mp4)

Azimuth angle effect to the brightness animated for 4 intrusion depths (mp4)

AUTHOR INFORMATION

Corresponding Author

*Email: yuning@ucla.edu

REFERENCES

(1) Xu, M.; Sun, G.; Kim, C.-J. Infinite lifetime of underwater superhydrophobic states. *Phys. Rev. Lett.* **2014**, *113*, 136103.

(2) Lee, C.; Choi, C.-H.; Kim, C.-J. Superhydrophobic drag reduction in laminar flows: a critical review. *Exp. Fluids* **2016**, *57*, 176.

(3) Rothstein, J.P. Slip on superhydrophobic surfaces. *Annu. Rev. Fluid Mech.* **2010**, *42*, 89-109.

(4) Xu, M.; Grabowski, A.; Yu, N.; Kerezyte, G; Lee; J.-W.; Pfeifer, B.R.; Kim, C.-J. Superhydrophobic drag reduction for turbulent flows in open water. *Phys. Rev. Appl.* **2020**, *13*, 034056.

(5) Golovin, K.B.; Gose, J.W.; Perlin, M.; Ceccio, S.L.; Tuteja, A. Bioinspired surfaces for turbulent drag reduction. *Philos. Trans. Royal Soc. A* **2016**, *374*, 20160189.

(6) Bixler, G.D.; Bhushan, B. Rice and butterfly wing effect inspired low drag and antifouling surfaces: a review. *Crit. Rev. Solid State Mater. Sci.* **2015**, *40*, 1-37.

(7) Ferrari, M.; Cirisano, F. Hydrophobicity and superhydrophobicity in fouling prevention in sea environment. In *Advances in Contact Angle, Wettablility and Adhesion*; Mittal, K.L., Ed.; John Wiley & Sons: Newark, NJ, USA, 2018; pp. 241-265.

(8) Brocher, F. Reserches sur la respiration des insects aquatiques adultes–les haemonia. *Ann. Biol. Lac* **1912**, *5*, 5-26.

(9) Cassie, A.; Baxter, S. Wettability of porous surfaces, *Trans. Faraday Soc.* **1944**, *40*, 546–551.

(10) Liu, T.; Chen, Z.; Kim, C.-J. A dynamic Cassie-Baxter model. *Soft Matter* **2015**, *11*, 1589-1596.

(11) Wenzel, R.N. Resistance of solid surfaces to wetting by water. *Ind. Eng. Chem. Res.* **1936**, *28*, 988–994.

(12) Crowdy, D.G. Analytical formulae for longitudinal slip lengths over unidirectional superhydrophobic surfaces with curved menisci. *J. Fluid Mech.* **2016**, *19*, 791.

(13) Biben, T.; Joly, L. Wetting on nanorough surfaces. *Phys. Rev. Lett.* **2008**, *100*, 186103.

(14) Teo, C.J.; Khoo, B.C. Flow past superhydrophobic surfaces containing longitudinal grooves: effects of interface curvature. *Microfluid. Nanofluidics* **2010**, *9*, 499-511.

(15) Bobji, M.S.; Kumar, S.V.; Asthana, A.; Govardhan, R.N. Underwater sustainability of the "Cassie" state of wetting. *Langmuir* **2019**, *25*, 12120-12126.

(16) Poetes, R.; Holtzmann, K.; Franze, K.; Steiner, U. Metastable underwater superhydrophobicity. *Phys. Rev. Lett.* **2010**, *105*, 166104.

(17) Samaha, M.A.; Tafreshi, H.V.; Gad-el-Hak, M. Influence of flow on longevity of superhydrophobic coatings. *Langmuir* **2012**, *28*, 9759-9766.

(18) Lee, J.; Zhang, Z.; Baek, S.; Kim, S.; Kim, D.; Yong, K. Bio-inspired dewetted surfaces based on SiC/Si interlocked structures for enhanced-underwater stability and regenerative-drag reduction capability. *Sci. Rep.* **2016**, *6*, 24653.

(19) Hokmabad, B.V.; Ghaemi, S. Effect of flow and particle-plastron collision on the longevity of superhydrophobicity. *Sci. Rep.* **2017**, *7*, 41448.

(20) Rathgen, H.; Mugele, F. Microscopic shape and contact angle measurement at a superhydrophobic surface. *Faraday Discuss.* **2010**, *146*, 49-56.

(21) Saad, N.; Dufour, R.; Campistron, P.; Nassar, G.; Carlier, J.; Harnois, M.; Merheb, B.; Boukherroub, R.; Senez, V.; Gao, J.; Thomy, V. Characterization of the state of a droplet on a micro-textured silicon wafer using ultrasound. *J. Appl. Phys.* **2012**, *112*, 104908.

(22) Dufour, R.; Saad, N.; Carlier, J.; Campistron, P.; Nassar, G.; Toubal, M.; Boukherroub, R.; Senez, V.; Nongaillard, B.; Thomy, V. Acoustic tracking of Cassie to Wenzel wetting transitions. *Langmuir* **2013**, *29*, 13129-13134.

(23) Li, S.; Lamant, S.; Carlier, J.; Toubal, M.; Campistron, P.; Xu, X.; Vereecke, G.; Senez, V.; Thomy, V.; Nongaillard, B. High-frequency acoustic for nanostructure wetting characterization. *Langmuir* **2014**, *30*, 7601-7608.

(24) Wang, P.; Su, J.; Shen, M.; Ruths, M.; Sun, H. Detection of liquid penetration of a micropillar surface using the quartz crystal microbalance. *Langmuir* **2017**, *33*, 638-644.

(25) Ichikawa, Y.; Yamamoto, K.; Yamamoto, M.; Motosuke, M. Near-hydrophobic-surface flow measurement by micro-3D PTV for evaluation of drag reduction. *Phys. Fluids* **2017**, *29*, 092005.

(26) Checco, A.; Ocko, B.M.; Rahman, A.; Black, C.T.; Tasinkevych, M.; Giacomello, A.; Dietrich, S. Collapse and reversibility of the superhydrophobic state on nanotextured surfaces. *Phys. Rev. Lett.* **2014**, *112*, 216101.

(27) Reholon, D. and Ghaemi, S. Plastron morphology and drag of a superhydrophobic surface in turbulent regime. *Phys. Rev. Fluids* **2018**, *3*, 104003.

(28) Flynn Bolte, K.T.; Balaraman, R.P.; Jiao, K.; Tustison, M.; Kirkwood, K.S.; Zhou, C.; Kohli, P. Probing Liquid–Solid and Vapor–Liquid–Solid Interfaces of Hierarchical Surfaces Using High-Resolution Microscopy. *Langmuir* **2018**, *34*, 3720-3730.

(29) Papadopoulos, P.; Mammen, L.; Deng, X.; Vollmer, D.; Butt, H.J. How superhydrophobicity breaks down. *Proc. Natl. Acad. Sci.* **2013**, *110*, 3254-3258.

(30) Lv, P.; Xue, Y.; Liu, H.; Shi, Y.; Xi, P.; Lin, H.; Duan, H. Symmetric and asymmetric meniscus collapse in wetting transition on submerged structured surfaces. *Langmuir* **2015**, *31*, 1248-1254.

(31) Lv, P.; Xue, Y.; Shi, Y.; Lin, H.; Duan, H. Metastable states and wetting transition of submerged superhydrophobic structures. *Phys. Rev. Lett.* **2014**, *112*, 196101.

(32) Kim, H.; Park, H. Diffusion characteristics of air pockets on hydrophobic surfaces in channel flow: Three-dimensional measurement of air-water interface. *Phys. Rev. Fluids* **2019**, *4*, 074001.

(33) Moosmann, M.; Schimmel, T.; Barthlott, W.; Mail, M. Air–water interface of submerged superhydrophobic surfaces imaged by atomic force microscopy. *Beilstein J. Nanotechnol.* **2017**, *8*, 1671-1679.

(34) Ghosh, U.U.; Nair, S.; Das, A.; Mukherjee, R.; DasGupta, S. Replicating and resolving wetting and adhesion characteristics of a rose petal. *Colloids Surf. A Physicochem. Eng. Asp.* **2019**, *561*, 9-17.

(35) Elbourne, A.; Dupont, M.F.; Collett, S.; Truong, V.K.; Xu, X.; Vrancken, N.; Baulin, V.; Ivanova, E.P.; Crawford, R.J. Imaging the air-water interface: Characterising biomimetic and natural hydrophobic surfaces using in situ atomic force microscopy. *J. Colloid Interface Sci.* **2019**, *536*, 363-371.

(36) Paxson, A.T.; Varanasi, K.K. Self-similarity of contact line depinning from textured surfaces. *Nat. Commun.* **2013**, *4*, 1-8.

(37) Yang, S.; Du, J.; Cao, M.; Yao, X.; Ju, J.; Jin, X.; Su, B.; Liu, K.; Jiang, L. Direct Insight into the Three-Dimensional Internal Morphology of Solid–Liquid–Vapor Interfaces at Microscale. *Angew. Chem.* **2015**, *54*, 4792-4795.

(38) Lim, S.J.; Kim, D.; Kim, Y.; Jeong, S.; Pang, C.; Ryu, S.; Weon, B.M. Hydrophobicity evolution on rough surfaces. *Langmuir* **2020**, *36*, 689-696.

(39) Rykaczewski, K.; Landin, T.; Walker, M.L.; Scott, J.H.J.; Varanasi, K.K. Direct imaging of complex nano-to microscale interfaces involving solid, liquid, and gas phases. *ACS Nano* **2012**, *6*, 9326-9334.

(40) Wiedemann, S.; Plettl, A.; Walther, P.; Ziemann, P. Freeze fracture approach to directly visualize wetting transitions on nanopatterned superhydrophobic silicon surfaces: more than a proof of principle. *Langmuir* **2013**, *29*, 913-919.

(41) Aljallis, E.; Sarshar, M.A.; Datla, R., Sikka, V.; Jones, A.; Choi, C.H. Experimental study of skin friction drag reduction on superhydrophobic flat plates in high Reynolds number boundary layer flow. *Phys. Fluids* **2013**, *25*, 025103.

(42) Xu, M.; Yu, N.; Kim, J.; Kim, C.-J. Superhydrophobic drag reduction in high-speed towing tank. *J. Fluid Mech.* **2021**, *908*, A6.

(43) Lee, C.; Kim, C.-J. Maximizing the Giant Liquid Slip on Superhydrophobic Microstructures by Nanostructuring Their Sidewalls. *Langmuir* **2009**, *25*, 12812-12818.

(44) Park, H.; Sun, G.; Kim, C.-J. Superhydrophobic turbulent drag reduction as a function of surface grating parameters. *J. Fluid Mech.* **2014**, *747*, 722-734.

(45) Yu, N.; Kim, C.-J. Detecting the sub-states of grating superhydrophobic surfaces with naked eyes. *Proc. IEEE Int. Conf. Micro Electro Mechanical Systems*, Belfast, U.K. **2018**, 1293-1295.

(46) Born, M. and Wolf, E. *Principles of optics*, 7th ed.; Pergamon Press Inc.: New York, 1999.

(47) Xu, M.; Liu, C.; Kim, C.-J. Self-powered plastron preservation and one-step molding of semi-active superhydrophobic surfaces. *Langmuir* **2020**, *36*, 8193-8198.

TOC Graphic: